IEEE Access
Multidisciplinary ⋮ Rapid Review ⋮ Open Access Journal

Received 10 November 2025, accepted 30 November 2025, date of publication 3 December 2025,
date of current version 9 December 2025.

Digital Object Identifier 10.1109/ACCESS.2025.3639809

APPLIED RESEARCH

Scan-to-QC: Quality Control of Prefabricated Structural Systems Using Point Clouds

REZA MAALEK[1] AND SHAHROKH MAALEK[2]
[1]Department of Digital Engineering and Construction (DEC), Karlsruhe Institute of Technology (KIT), 76131 Karlsruhe, Germany
[2]Iranian Institute of Spatial Structures (IISS), Tehran 11155-4563, Iran

Corresponding author: Reza Maalek (reza.maalek@kit.edu)

ABSTRACT Background: The use of point clouds to perform quality control (QC) of prefabricated structural systems is growing markedly. The sustained application of point clouds on construction projects at scale, however, requires reliable and automated frameworks to foster practicality. Literature Review: Existing solutions seldom incorporate the impact of instrument artifacts, construction errors, and complex element geometries, rendering the frameworks error-prone and sensitive to thresholds, outliers, and missing data. More specifically, current methods: 1) are not generalizable to any freeform element; 2) rely on local primitives, which increases runtime and threshold subjectivity; 3) do not formulate the point cloud to model fitting based on geometric distance; and 4) do not incorporate a dedicated outlier detection to explicitly handle large outliers. Methodology: This study presents, scan-to-QC, a generic solution for automatic QC of prefabricated elements with non-analytic cross-sections using point clouds. The framework addresses the current state-of-the-art limitations (above) by providing a generic, direct artificial-intelligence (AI)-based geometric distance fitting robust to outliers. The proposed approach introduces four new algorithms to: 1) represent the cross-sectional boundaries of elements with trigonometric polynomials, 2) perform orthogonal fitting of points to these polynomials, 3) remove outlying observations through robust concentration steps (CS), and 4) perform assembly verification of prefabricated elements in construction projects. As the convergence of CS depends on the initial fitting parameters, the performances of seven deterministic, heuristic, and AI-based (i.e., metaheuristic and global computational intelligence-based) optimization strategies to recover these parameters were evaluated on point clouds of five common prefabricated elements with complex geometries. The comparative analysis considered factors such as the fit quality, object detection accuracy, and computation runtime. Results and Conclusions: Among these methods, the Particle Swarm (PS) achieved the best results, significantly outperforming Simulated Annealing, Bayesian, and Genetic Algorithm. Furthermore, by fine-tuning the swarm size, the PS attained 99% and 96% accuracies in object detection and fitting quality, respectively. Finally, the calibrated PS algorithm was applied to the point cloud of a real-world prefabricated spaceframe structure, yielding 98.5% reliability in nodal coordinate estimation compared to the ground truth.

INDEX TERMS Building automation, building information management, metaheuristics, total quality management, prefabricated construction.

I. INTRODUCTION

A. PREFABRICATION QUALITY CONTROL

The global prefabricated construction market has experienced substantial growth since the year 2020. Projected at \$153.7 billion in 2026, [1] with a compound annual growth rate (CAGR) of around 7%, driven by the desire to achieve faster construction, address skilled labor shortages, and promote sustainable practices. Multiple studies have reported the potential of prefabricated construction to reduce cost, duration, material waste, energy consumption, and carbon emissions compared to conventional methods, as follows:

- Cost reduction of 10% in the European Union (EU) [2]
- Timesaving of 20–50% [3], [4]

The associate editor coordinating the review of this manuscript and approving it for publication was Shih-Wei Lin.

- Material waste reduction of 52% [5]
- Life-cycle energy consumption reduction of 4–14% [6]
- Carbon emission reduction of 4–20% in the USA [7].

Prefabricated construction capitalizes on the advantages offered by controlled and precision manufacturing processes, such as lean practices and total quality management. However, unlike in the manufacturing industry, where the entire asset can be built under controlled settings, prefabricated construction requires on-site assembly and installation of either prefabricated individual elements (e.g., structural elements) or off-site modular elements (e.g., industrial modules [8]). Therefore, the potential risks associated with human errors during assembly cannot be neglected. For instance, human errors during the construction of prefabricated bridges have reportedly contributed to 6–17% of bridge collapses [9]. If these assembly errors are not found or reported on time, they constitute omission errors, contributing to approximately 38% of the costly rework [10].Therefore, this study proposes a generic framework for the quality control of prefabricated elements with arbitrary cross sections from point clouds, referred to as scan-to-QC for brevity.

B. COMPLEXITY OF AUTOMATIC SCAN-TO-QC

The automatic processing of point clouds in construction projects involves assigning each point to its corresponding real-world object to derive relevant construction analytics. Point cloud processing is challenging due to various data artifacts, such as missing data from occlusions and outlying observations, geometric disparities between the built and planned structures caused by construction errors, and incomplete or inaccurate planned baseline information [11]. Based on this, the following three construction project-specific categories of error can contribute to the complexities associated with point cloud processing:

- *point cloud errors* (e.g., instrument errors, such as random, systematic, and registration errors, along with scene-specific data artifacts, such as mixed pixels and incidence angle errors);
- *construction errors* (e.g., human errors, such as dimensioning, floor levelness and assembly errors); and
- *planned information errors* (e.g., incompleteness and/or errors in graphical, textual, and semantic planned information).

To provide further perspective, point clouds with higher instrument accuracy and/or resolution from known sources–i.e., with quantifiable measurement uncertainty–are less complex to analyze than those acquired using unknown instruments. Similarly, the processing of point clouds acquired from construction projects with lower or quantifiable construction errors–e.g., through controlled robotic fabrication and assembly methods–is easier compared to construction projects where the existence of considerable construction errors cannot be ruled out. Finally, processing point clouds for a construction project with limited baseline planned information is inherently more complex than for projects with a detailed semantic digital model–e.g., created through the building information modeling (BIM) process–which can limit the search space and guide the object detection process. As such, a strategy for automatically processing point clouds must account for the unique challenges posed by these three categories of errors.

C. STUDY SCOPE AND PROBLEM FORMULATION

Prefabricated elements are assumed to undergo quality control before assembly, either on-site or off-site; hence, the dimensional errors of the elements can be modeled based on tolerances. However, significant installation/assembly errors owing to element placement, position, and orientation remain possible. Figure 1a shows the registered point cloud and digital model of a hollow structural section (HSS) member, illustrating considerable assembly error. Figures 1b and 1c show the results of the point cloud tolerance checking using the commercial software Verity and the proposed method described in this manuscript, respectively. As observed, Verity, using the default settings, could not identify the correct correspondences between the model and point cloud, likely because of substantial outlying observations. In contrast, the proposed method correctly determined the point-to-model correspondences. Therefore, the desired automated scan-to-QC method must be adaptable to different conditions, such as noise levels and outlier ratios, to accurately quantify the level of noncompliance.

For further context, Verity is a commercial software that performs QC within the Autodesk Navisworks environment as a plugin. As such, it is interoperable with current BIM exchange formats, such as issue foundation class (IFC) particularly those acquired from software suites such as Revit and Tekla. Furthermore, temporal point clouds can be connected directly with 4D simulations, obtained from interoperable suites, such as Navisworks. Similarly, the proposed scan-to-QC methodology can also connect to existing BIM workflows by improving the QC accuracy as depicted in Figure 1. The accurate reporting of the QC reduces manual validation of the results and increases the reliability of the tolerance checking report.

The conceptual diagram demonstrating the relationship between the input layers (i.e., point cloud and BIM), the analysis layer (i.e., scan-to-QC), and the analytics layer (generation of geometric digital twins [12]) is demonstrated in Figure 1d. The input layer includes the point cloud and BIM. The BIM represents the baseline geometry and elements required for detection along with their tolerances. The scan-to-QC layer involves the initial point cloud to BIM registration, followed by BIM element detection and construction error estimation. This information is then fed to the analytics layer, where relevant analytics such as the geometric digital twin as well as tolerance classes (in terms of severity) are generated.

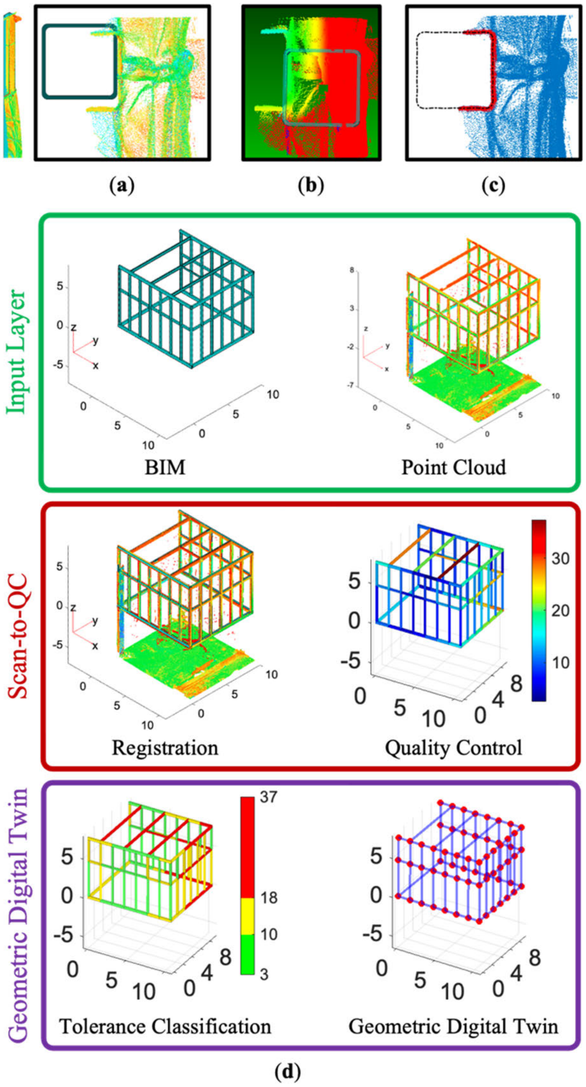

FIGURE 1. Prefabricated steel element with assembly error: (a) registered point cloud and digital model 3D (left) and 2D (right); and point cloud processing for quality control: (b) Verity and (c) proposed method. (d) Depicts the relation between input layer (point cloud and BIM), analysis layer (scan-to-QC), and analytics layer (geometric digital twin).

D. MODEL-BASED POINT CLOUD PROCESSING

Bosché [13], [14] presented a template matching solution, scan vs. BIM (SvB), using a combination of frustum-based ray-casting, iterative closest point (ICP) registration or its many variants, [15] and random sample and consensus (RANSAC) planar outlier detection. The primary advantage of this method is its simplicity, and other than RANSAC [16], the remainder is deterministic. However, the accuracy of the method depends heavily on the magnitude of the predefined distance threshold D_{Thresh} [13], [17]. Furthermore, ICP cannot guarantee the recovery of transformation parameters for large transformations.

Extensions to the original SvB (e.g., utilizing local curvature analysis [18]) have proven effective, particularly for smooth and curved surfaces, including planes (PvB in [17]) and pipes [19], [20], [21]. However, local curvature analysis requires an optimal neighborhood definition, which can only be solved heuristically by employing either Monte Carlo sampling [22] or artificial intelligence (AI)-based approaches such as Bayesian methods [23]. These methods also require an adaptive threshold to check the agreement between the local curvature of the BIM and point clouds. This requires either reliable closed-form solutions for the propagation of measurement uncertainty to predict the curvature estimation uncertainty, [18] or sufficient historical data to train machine learning models, such as support vector machines (SVM) [23]. However, these approaches increase complexity and computation time.

Another approach relies on direct fitting of the model to the point cloud. After an initial registration between the digital model and point cloud, a loose neighborhood around each element is defined to encompass the points of the desired element. The latter can also be achieved through object classification [24] and instance segmentation [25], [26]. The goal is to fit the geometric model of the elements onto the inlier points. Commonly suitable for elements with analytic geometries, such as planes, spheres, and cylinders, this approach combines least-squares fitting with robust outlier detection. Robust statistical methods consist of an initial estimation of the model parameters followed by iterative outlier removal, referred to as the concentration step (CS). To avoid local convergence, the performance of these methods depends on the accurate estimation of the initial model parameters [27]. This also holds for methods that rely on grid occupancy of the element's cross-section to find corresponding points [28] as they require an accurate estimation of the initial element's axis [8]. Monte Carlo-based random sampling strategies have been proposed [29] to obtain at least one outlier-free set of observations. Monte Carlo-based methods, however, are heuristic and depend on the number and size of random samples [30], [31].

To reduce the impact of the results on the randomness of the initial parameter estimation, AI-based global optimization methods [32], such as Bayesian [33], Genetic Algorithm (GA) [34], Simulated Annealing (SA) [35], and Particle Swarm (PS) [36], can be employed to provide systematic strategies that help recover the initial model-fitting parameters. These global optimization methods are also effective for solving both least trimmed squares (LTS) and least median of squares (LMS) problems in contaminated datasets (e.g., Bayesian [37], Genetic [38], SA [39], and PS [40]).

Metaheuristic optimization was incorporated within recent studies in construction informatics to fit polygonal approximation models to points. These included the utilization of (i) mean squared error (MSE) to fit disjoined polygon lines to boundary points in bridge infrastructure [41], and (ii) logarithm of Root-MSE (RMSE), relative edge length, and relative surface normal between point and model in steel structure [25], [42]. While these methods show effectiveness on the example datasets, they in their current form: (i) are not generalizable to any freeform; (ii) rely on curvature analysis to define the objective function, which increases runtime and subjectivity; (iii) do not formulate RMSE based on geometric distance; and (iv) do not incorporate CS to explicitly handle large outlier ratios.

This manuscript proposes the problem of detecting BIM/CAD elements from point clouds–within a flexible boundary around the element–as the solution to an AI-based robust model-fitting process. The proposed method avoids the need for local curvature analysis. Furthermore, the method is sufficiently flexible to detect elements with cross-sections of any shape, even in the presence of outlying observations.

Table 1 presents a summary of the comparisons between the proposed and available methods in the construction informatics literature. The content of this table shows that the proposed approach builds on the scientific findings presented in current literature by: (i) offering a direct point cloud model fitting suitable to any cross-section geometry; (ii) using a new closed-form geometric distance formulation of points to free-form curves; and (iii) applying a dedicated robust outlier removal strategy for large outlier ratios.

TABLE 1. Summary of state-of-the-art in direct model fitting.

Study	BIM geometry	Objective function	Outlier removal	Optimization Solution
[43]	NURBS	RMSE	X	Least squares (LS)
[13]	Disjoined polygon	RMSE	RANSAC (subjective)	ICP
[41]	Disjoined polygon	MSE	X	TLBO, but solvable with LS
[25]	Continuous polygon	log(RMSE) edge length normal comparison	X	PS, reliant on local curvature
Ours	Any parametric curve	RMSE coverage density	Robust CS	PS, GA, SA, Bayesian, closed geometric fitting

E. STUDY OBJECTIVES

The objective of this study is to provide a generic solution to the fitting of prefabricated elements (i.e., elements adhering to production-line dimensional quality control standards) with non-analytic cross-sections to point clouds in the presence of outlying observations and considerable on-site (or off-site) construction assembly errors. Furthermore, while not explicitly investigated, the methodology is flexible enough to incorporate small structural deformations under construction loads and elements with variable cross-sectional areas.

To achieve this, the sub-objectives of the study are to:

- *Formulation*: reformulate the problem of point cloud detection of prefabricated elements of any shape into robust model fitting–instead of relying on popular template matching methods–through:
    - ∘ *Cross-section parameterization:* represent the cross-sectional area of arbitrarily shaped elements with a double-differentiable continuous parametric equation
    - ∘ *Geometric fitting:* derive the new equations required to fit the parametric model to points, including:
        - ▪ *Orthogonal contact point:* establish the mathematical bases to formulate the orthogonal contacting point to model
        - ▪ *Best fit:* derive gradient-based optimization to find the best-fit parameters
    - ∘ *AI optimization:* apply metaheuristic algorithms, such as Particle Swarm (PS), Genetic algorithm, Simulated Annealing (SA), and Bayesian optimization, to find initial fitting parameters
    - ∘ *Robust outlier removal:* develop new robust CS to adaptively remove substantial outliers from data during fitting
- *Verification*: evaluate the suitability of the proposed point cloud fitting method on a selected set of prefabricated structural steel elements with different cross-section types, such as W-section, rectangular HSS, and C-section, assessing object detection quality, fitting accuracy, and computation time
- *Validation*: quantify the reliability and performance of the method with the best-performing results for assembly verification of prefabricated steel members from a real-world space frame structure.

II. METHODOLOGY

The method to solve the point cloud processing of prefabricated and quality-controlled elements in the presence of large construction assembly errors involves three main steps, as depicted in Figure 2 and *Algorithm 1: Scan-to-QC of Prefabricated Elements*. Steps 1 and 3 of Algorithm 1 were adopted from [8]. Here, the algorithm was further refined to: (i) include elements with non-analytic cross-sections, such as W–Sections, through parametric function approximation; (ii) derive the mathematical bases to fit point clouds to the derived parametric function; and (iii) systematically reduce the possibility of local convergence of robust CS by employing AI-based optimization robust to considerable assembly errors.

A. ORTHOGONAL FITTING OF PARAMETRIC FUNCTIONS TO POINT CLOUDS

In this study, the derived model formulates the shortest (orthogonal) distance from a point to the curve, referred to as the geometric (orthogonal) distance. Given the parametric equation of the boundaries of CAD/BIM of the element, the generic equations for the orthogonal fitting of points to the parametric equation are derived as follows:

$$D_{X,Y,t} = \left\| \begin{bmatrix} D_X \\ D_Y \end{bmatrix} \right\| = \left\| \begin{bmatrix} X - X_I \\ Y - Y_I \end{bmatrix} \right\| = \left\| \begin{bmatrix} X - f_{X,t} \\ Y - f_{Y,t} \end{bmatrix} \right\| \quad (1)$$

where $D_{X,Y,t}$ is the distance function; $\|.\|$ denotes the L2-norm; (D_X, D_Y) represents the distance in X

Algorithm 1 Scan-to-QC of Prefabricated Elements

```
INPUT:  3D POINT COORDINATES, $(x, y, z)_i$: $i \in \{1, 2, \ldots, N\}$, TERMS OF PARAMETRIC
        FUNCTION,
        $(f_{X,t}, f_{Y,t})_k : k \in \{1, 2, \ldots, L\}$, REPRESENTING THE
        BIM ELEMENT TYPE BOUNDARIES, AND
        NEIGHBORHOOD THRESHOLD, $1 < \delta_N < 2$.
OUTPUT: ELEMENT'S ASSEMBLY ERROR, $\hat{\sigma}_{El_k} : k \in \{1, 2, \ldots, L\}$.

1. Register     Perform target-based registration between point
                cloud and BIM through pre-surveyed control points (Figure 2a).
2. Detect       For each BIM element in $k \in \{1, 2, \ldots, L\}$, perform
                the following steps:
  2.1. Select       Select points within element bounding box
                    isometrically scaled by $\delta_N$ (Figure 2b);
  2.2. Transform    Orient the point cloud so that the BIM element's
                    axis aligns with the z-axis (Figure 2b);
  2.3. Fit Model    Perform AI-based model fitting on the
                    transformed point cloud in the x-y plane to
                    recover transformation parameters (Figure 2c);
  2.4. Robust Fit   Perform Algorithm 3 on the transformed points
                    from Step 2.3 to determine the inlier points and
                    final transformation parameters (Figure 2d);
  2.5. Fit Error    Calculate the RMSE between the inlier points
                    before and after transformations of Steps 2.3
                    and 2.4 and store as the assembly error, $\hat{\sigma}_{El}$.
3. Analytics    Color-code the results for each element based on
                the estimated $\hat{\sigma}_{El}$ and standard code of
                practice, or k-means clustering (Figure 2e).
```

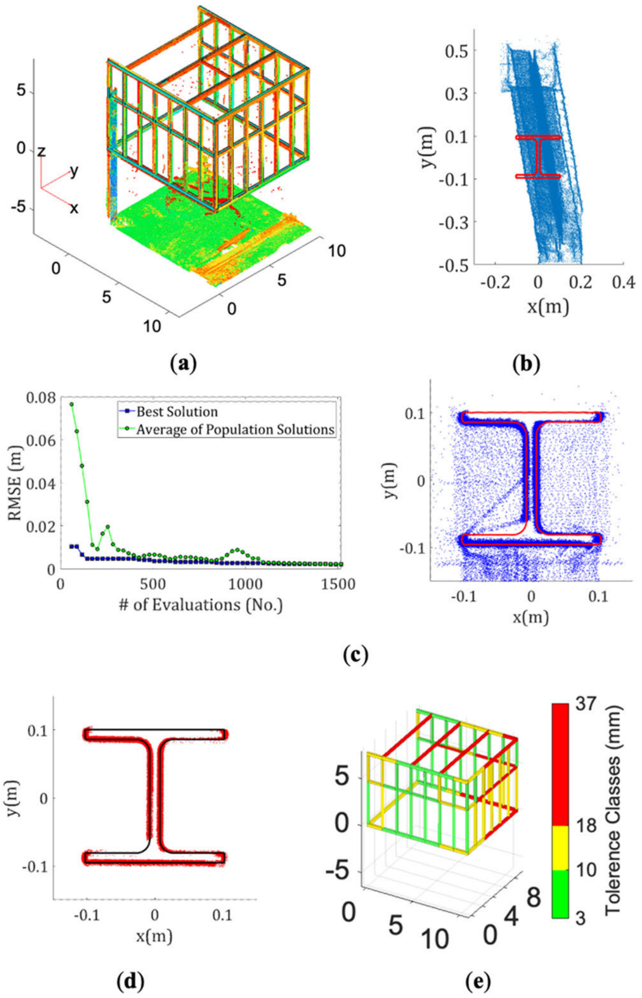

FIGURE 2. Schematics of the proposed scan-to-QC: (a) point cloud and model registration; (b) selected points around element, axis-aligned with z and projected onto the x-y plane; (c) AI-based fitting: convergence–left, and final rotated points–right; (d) detected outliers after robust CS; and (e) color-coding into three tolerance severity classes using k-means.

and Y axes; $X = (x - x_c)\cos\theta + (y - y_c)\sin\theta, Y = -(x - x_c)\sin\theta + (y - y_c)\cos\theta$, $\rho = (x_c, y_c, \theta)$ are the geometric parameters of the best fit onto the points (x, y), (X_I, Y_I) are the orthogonal contacting points; and $(f_{X,t}, f_{Y,t})$ are the parametric representations of the orthogonal contacting point. Following Ahn's geometric orthogonal least-squares fit for ellipses [44], the problem is divided into two main subsections: (i) estimation of the orthogonal contacting point $(X_I, Y_I) = (f_{X,t}, f_{Y,t})$; and (ii) minimizing the sum of the squared distances between points and its orthogonal contacting point.

B. FORMULATING THE ORTHOGONAL CONTACTING POINT

The orthogonal contacting point corresponding to point (X, Y) must satisfy the following condition:

$$\frac{df_{Y,t}}{df_{X,t}} \cdot \frac{Y - Y_I}{X - X_I} = -1 \tag{2}$$

where $\frac{df_{Y,t}}{df_{X,t}}$ denotes the gradients of the parametric function at the orthogonal contact point. By employing the chain rule in differential calculus, the equation can be simplified as:

$$g_{X,Y,t} = f'_{Y,t} \cdot \left(Y - f_{Y,t}\right) + f'_{X,t} \cdot \left(X - f_{X,t}\right) = 0 \tag{3}$$

where $(f'_{X,t}, f'_{Y,t})$ are the derivatives of $(f_{X,t}, f_{Y,t})$ with respect to the parameter t. The orthogonal contact point is estimated through gradient-based minimization (here, Gauss-Newton) as follows:

$$\min_t g^2_{X,Y,t} \xrightarrow{Gauss-Newton} \tag{4}$$

$$\rightarrow \begin{cases} \dfrac{dg_{X,Y,t}}{dt} = g'_{X,Y,t} \\ \delta t = -\left.\dfrac{g_{X,Y,t}}{g'_{X,Y,t}}\right|_{t=t_j} \\ t_{j+1} = t_j + \delta t \end{cases} \tag{5}$$

where $g'_{X,Y,t}$ is the derivative of $g_{X,Y,t}$ with respect to t, δt is the Gauss-Newton correction; t_j is the decision variable at iteration j, and $(f''_{X,t}, f''_{Y,t})$ are the second derivatives of $(f_{X,t}, f_{Y,t})$ with respect to t.

III. FITTING PARAMETRIC EQUATIONS TO POINTS

Given the orthogonal contacting point, the geometric parameter vector $\rho = (x_c, y_c, \theta)$, can now be estimated by minimizing the following least-squares objective function:

$$\min_\rho \sum_{i=1}^{N} {D_{X,Y,t_i}}^2 = \sum_{i=1}^{N} \left({D_{X,t_i}}^2 + {D_{Y,t_i}}^2\right) \tag{6}$$

Equation (6) is a nonlinear problem, but so long as the Jacobian can be analytically derived, it is solvable using iterative gradient-based methods such as Levenberg-Marquardt [31]. The Jacobian of the objective function with respect to the geometric parameter vector $\rho = (x_c, y_c, \theta)$ is presented in Appendix A in closed-form. Equations (1)–(6), along with those presented in Appendix A, provide the mathematical bases to fit a parametric equation of a curve with the CAD/BIM boundary represented by the parametric function $(f_{X,t}, f_{Y,t})$ to neighboring points. Based on the derived equations, this parametric function must be (i) represented by one parameter, t; and (ii) continuous and double-differentiable in $\Re$. In the following section, trigonometric polynomials (TPs) are selected as suitable parametric functions.

A. TRIGONOMETRIC APPROXIMATION OF BIM

Parametric equations are formulations where points are represented as a function of an auxiliary variable, t, referred to as the parameter. The parametric representation is suitable for closed curves, where an injective function in implicit form cannot be generated. Different strategies for parametrization, such as arc length, trigonometric (or cyclical/angular), and Bézier, can be employed depending on the complexity of the shape of the curve. Once an effective parameterization strategy is chosen, a parametric function can be generated to map a set of points–in our case from the boundaries of the BIM element in 2D (X_{BIM}, Y_{BIM})–onto $(f_{X,t}, f_{Y,t})$. This mapping is synonymous with a regression problem (generally non-linear) in the orthogonal Cartesian axes.

These regressions can be formulated without prior knowledge through recent developments in symbolic regression (SR), which uses evolutionary programming to find the best fit function in terms of parsimony, accuracy, and complexity, or through available formulations such as rational splines or TPs. On the one hand, the SR problem is NP–hard; on the other hand, additional constraints must be defined within the SR method to guarantee the continuous and double differentiability requirements of the resulting function imposed by Equations (1)–(6).

Previous studies have utilized rational splines, such as non-uniform rational B-spline (NURBS), to parameterize the boundaries of CAD/BIM elements. NURBS are effective in generating accurate formulations even for sharp curve boundaries. This property, however, will not benefit direct point cloud model fitting due to incidence angle error artifacts at sharp edges. NURBS are constructed through the ratio of two splines. As such, the general guarantee of differentiability and continuity require effective weighting strategies to prevent division by zero.

Another approach is to utilize epicycle mathematics by fitting a trigonometric Fourier series (infinite series) to the points. This form of trigonometric series satisfies all the requirements mentioned in the previous section and its utility has been well-established within the literature [45], [46]. However, while the infinite series is exact, it lacks parsimony. In fact, as the number of terms of series l, increases, the agreement between the continuous function and boundaries also increases. In this study, TP approximation is utilized due to flexibility, effectiveness in capturing round curves, and numerical stability; however, the provided formulations are agnostic to the type of parameterization, and can easily be adjusted for other function types, such as NURBS.

Algorithm 2: Trigonometric BIM Approximation is developed to determine the TP function that achieves the desired RMSE agreement (σ_{Thresh}) between the boundary points and the final function by iteratively adding extra terms to the TP approximation.

Algorithm 2 Trigonometric BIM Approximation

```
INPUT:   DESIRED PRECISION, $\sigma_{Thresh}$, BIM/CAD BOUNDARY POINTS, AND $(X_{BIM}, Y_{BIM})_i$: $i \in \{1, 2, \ldots, M\}$.
OUTPUT:  BEST FIT TP PARAMETERS, $(f_{X,t}, f_{Y,t}) \equiv (a_{kX}, b_{kX}, a_{kY}, b_{kY}) : k \in \{1, 2, \ldots, l\}$.

1. Order   Cyclically order the boundary points by solving the traveling salesman problem (TSP) [47].
2. Terms   Calculate the terms of Fourier, $a_k$ and $b_k$ to form the parametric function $(X_t, Y_t) = (f_{X,t}, f_{Y,t})$ using Equation (7).
3. Error   Calculate the RMSE between original points and parameters.
4. Check   If $RMSE < \sigma_{Thresh}$,   retain the solution
           Else                    ,   go to step 2
```

The following sets of equations, Equation (7), are utilized within Algorithm 2. Based on these formulations and algorithms, the best-fit parameters were estimated using the Levenberg-Marquardt algorithm of [31]. The closed-form derivatives of the TP function in Equation (7) are provided in Appendix B.

$$\left\{\begin{array}{l} t_i = 2\pi \dfrac{i-1}{M-1}, i \in \{1, 2, \ldots, M\} \\ a_k = \dfrac{1}{2\pi} \sum_{i=1}^{M-1} X_{BIM_i} \cdot (t_{i+1} - t_i) \cdot \cos(kt_i) \\ b_k = \dfrac{1}{2\pi} \sum_{i=1}^{M-1} X_{BIM_i} \cdot (t_{i+1} - t_i) \cdot \sin(kt_i) \\ X_t = f_{X,t} = \sum_{k=1}^{l} a_{k_X} \sin(kt) + b_{k_X} \cos(kt) \\ Y_t = f_{Y,t} = \sum_{k=1}^{l} a_{k_Y} \sin(kt) + b_{k_Y} \cos(kt) \end{array}\right. \tag{7}$$

B. ROBUST OUTLIER REMOVAL

With the assumption that the orientation and translation are only applied in the 2D plane of the element's cross-section, *Algorithm 3: Robust Concentration Step* was employed to remove the outliers.

In this study, $\sigma_M = 10$ mm was sufficient to account for the geometric milling cross-sectional tolerances, fabrication camber and sweep tolerances, and point cloud measurement uncertainties for all element types; however, larger thresholds may be necessary, depending on the element and point cloud

Algorithm 3 Robust Concentration Step

```
INPUT:    TRANSFORMED 2D POINT COORDINATES OF STEP 2.2.
          IN ALGORITHM 1, $(x, y)_i : i \in \{1, 2, \ldots, N\}$, TERMS OF
          TP FUNCTION FROM ALGORITHM 2, $(f_{X,t}, f_{Y,t})$, and
          TOLERANCE THRESHOLD, $\sigma_M$.
OUTPUT:   INLIER POINTS, $ID = \{ i \in \mathbb{N} | w_i = 1, 1 \leq i \leq N$,
          AND BEST FIT PARAMETERS, $\rho = (x_c, y_c, \theta)^T$ .

1. TP Fit        Fit the TP function to points using the above
                 methods (Section II-A).
2. Residuals     Calculate the residuals for each observation from
                 the best fit.
3. Regularize    Regularize the observations using Equation (8).
4. Weight        Weight the observations using Equation (9).
5. Check         Iterate steps 1-4 until the weight vector between
                 two iterations remains unchanged
```

errors. The following equations are recalled in the algorithm.

$$Z_i = \frac{r_i - \underset{i \in \{1..N\}}{mode}(r_i)}{min\left(\underset{i \in \{1..N\}}{MADN}(r_i), \sigma_M\right)} \tag{8}$$

where $\underset{i \in \{1..N\}}{\text{mode}}(r_i)$ was estimated using the mean shift algorithm [48] and $\underset{i \in \{1..N\}}{\text{MADN}}(r_i)$ is the normalized mean absolute deviation about the median [49].

$$w_i = \begin{cases} 1, & |Z_i| \leq \sqrt{\chi^2_{2,0.95}} = 2.447 \\ 0, & |Z_i| > 2.447 \end{cases} \tag{9}$$

C. AI-BASED MODEL FITTING

Here, the goal of employing the evolutionary algorithm, swarm intelligence, and other nature-inspired model fitting was to provide a "good" initial estimation of the parameters, namely, the 3D rotation and translation, which can be represented by three Euler angles $(\omega, \varphi, \theta)$, and three translation parameters (x_c, y_c, z_c). To this end, the following objective function was formulated (10) and (11), as shown at the bottom of the page, where w_i is calculated using Equation (9) by performing the CS only once at each optimization evaluation step; $\left(f_{X_i,t_i}, f_{Y_i,t_i}\right)$ is the orthogonal projection of the rotated points (X_i, Y_i) onto the TP function; b represents the set of M original boundary points of the BIM/CAD element (see Section II-B); p represents the set of inlier points (i.e., those with $w_i = 1$); $\delta(b, p)$ is a function representing the number of unique nearest neighbors of p within b; C is a user-specified threshold representing the minimum acceptable coverage of the element; ε is a small number (0.001); and $\bar{\gamma}(p, b)$ is the function representing the average of the number of repetitions of all points in p nearest to those in b.

D. VALIDATION METRICS

The percentage of the ratio between the final RMSE and ground truth RMSE ($R_{RMSE\%}$), along with relevant object detection metrics, precision, recall, accuracy, and $F_{Measure}$, [50] of the final set of inlier points compared to the ground truth are calculated as follows:

$$\begin{cases} R_{RMSE\%} = \dfrac{R_{MSE_{Gt}}}{RMSE_{In}} \\ Precision_{\%} = \dfrac{t_p}{t_p + f_p} \\ Recall_{\%} = \dfrac{t_p}{t_p + f_n} \\ Accuracy_{\%} = \dfrac{t_p + t_N}{t_p + t_n + f_p + f_n} \\ F_{Measure\%} = 2 \cdot \dfrac{Precision.Recall}{Precision + Recall} \end{cases} \tag{12}$$

where $RMSE_{Gt}$ and $RMSE_{In}$ are the RMSE of the inlier points using the ground truth and the proposed method, respectively, and t_p, t_n, f_p, f_n are the true positive, true negative, false positive, and false negative of the detected inlier points, respectively. For consistency and ease of interpretation, here, the $R_{RMSE\%}$ is reported (instead of the nominal RMSE) so that 100% indicates the best result in all metrics.

IV. EXPERIMENTAL DESIGN

Two sets of experiments were conducted. The first involved evaluating seven methods for recovering the geometric parameters of five common prefabricated elements acquired from real construction sites in 1,000 different random orientations and translations. The second experiment was designed to verify the applicability of the best method from Experiment #1 for the assembly verification of the elements of a real-world cantilever spaceframe structure using Algorithm 2. Figure 3 shows the 3D point cloud and the models used in

$$\underset{(\omega,\varphi,\theta,x_C,y_C,z_C)}{min} \frac{\eta_A}{\tau_D \cdot \varphi_C} \tag{10}$$

$$\begin{cases} \eta_A = \dfrac{\sum_{-1}^{N} w_i \left(\left(x_i - f_{x_i,c_i}\right)^2 + \left(y_i - f_{y_i,c_i}\right)^2\right)}{\sum_{i=1}^{N} w_i}, & \begin{bmatrix} X_i \\ Y_i \\ Z_i \end{bmatrix}^T = \begin{bmatrix} x_i - x_c \\ y_i - y_c \\ z_i - z_c \end{bmatrix}^T \cdot R(\omega, \varphi, \theta) \\ \varphi_C = \begin{cases} 1 & \dfrac{\delta(b, p)}{M} \geq C \\ \varepsilon & \dfrac{\delta(b, p)}{M} < C' \end{cases} & b = \left\{(X_{BIM}, Y_{BIM})_j \mid j = 1 \ldots M\right\} \\ \tau_D = \bar{\gamma}(p, b) \cdot \dfrac{M}{N}, & p = \{(X_i, Y_i) \mid w_i = 1 \& i = 1 \ldots N\} \end{cases} \tag{11}$$

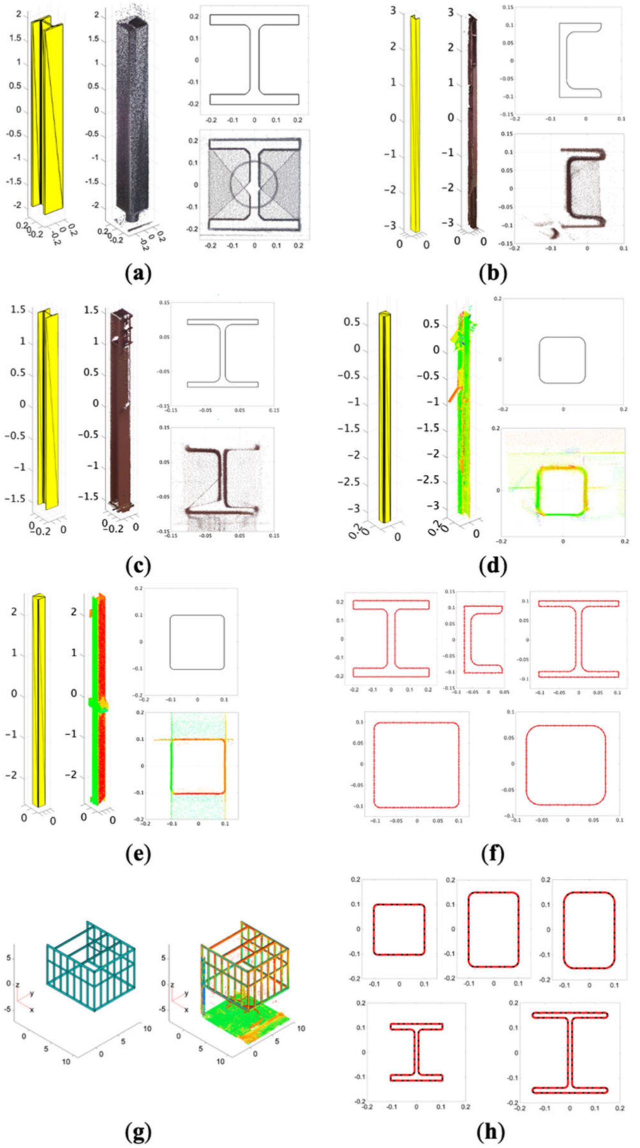

FIGURE 3. Experiment #1 (a)–(f): 3D model (left); 3D point cloud (middle); 2D plot (top-right); and 2D projected point cloud (bottom-right). (f) TP approximation. Experiment #2: (g) 3D BIM (left) and superimposed 3D point cloud (right); and (h) TP approximation of onsite elements.

the two experiments with Figures 3a–3f and Figures 3g–3h belonging to Experiments #1 and #2, respectively.

A. EXPERIMENT #1: INDIVIDUAL PREFABRICATED ELEMENTS

B. I. EXPERIMENT #1: SETUP

Seven different methods, namely deterministic methods of ICP and PvB, heuristic method of SvB, and metaheuristic methods of Bayesian, Genetic, SA, and PS, were implemented, and their performances in recovering the initial geometric parameters were compared. Table 2 summarizes the methods used in this study, the studies adopted for implementation, and tunable parameters outside the default parameters from the standard functions of MATLAB's Optimization Toolbox.

TABLE 2. Summary of considered methods with properties.

Method	Category	Tunable Thresholds
Iterative Closest Point (ICP)	Deterministic	$D_{thresh} = 0.2\text{m}$ $\Delta RMSE_{thresh} = 10^{-5}m$
Point Cloud vs. BIM	Deterministic	$D_{thresh} = 0.2\text{m}$
Scan vs. BIM (SvB)	Heuristic	$D_{thresh} = 0.2\text{m}$ $\Delta RMSE_{thresh} = 10^{-5}\text{m}$
Baysian [52], [53]	Metaheuristic/ Proposed methodology Section II	$C = 0.5$: Equation (10)–(11)
Genetic Algorithm [54], [55]		$\sigma_M = 0.01\text{m}$ (Algorithm III)
Simulated Annealing [56]		Max evaluations: 100,000
Particle Swarm [36], [57], [58]		$G_n^* \in \{10,15,20,25,30,40 \ldots$ $\ldots 50,75,100,150\}$

$^*G_n$, not applicable in Bayes, defines the population size in Genetic, swarm size in PS, and reannealing step in SA.

V. EXPERIMENT #1: GROUND TRUTH

For each of the elements used in this experiment (Figures 3a–3f), the points following the pattern of the best-fit TP function were determined using brute-force by applying a visual manual registration in CloudCompare, followed by evaluating 100^6 uniform combinations for $(\omega, \varphi, \theta, x_c, y_c, z_c)$ with $-0.5° \leq \omega, \varphi, \theta \leq 0.5°$ and $-0.005\text{m} \leq x_c, y_c, z_c \leq 0.005\text{m}$. Algorithm 3 was applied to each of the combinations and that achieving the lowest RMSE was chosen as the ground truth. The results of the brute-force ground-truth parameter estimations are summarized in Table 3.

TABLE 3. Experiment #1: Summary of ground truth.

Element ID	# of Points	Inlier RMSE (mm)	Outliers (%)	Coverage (%)
Figure 3a	107,664	2.9	27.3	98.8
Figure 3b	104,422	2.4	15.4	70.5
Figure 3c	89,360	2.3	17.9	75.6
Figure 3d	93,341	1.8	20.8	85.7
Figure 3e	111,402	1.3	9.2	93.6

A. EXPERIMENT #2: REAL-WORLD SPACEFRAME

The portion of the site under investigation (Figure 3g) included approximately 13.3 million points from three scan stations, with an overall registration precision of 1.2 mm. Algorithm 1 was applied to the entire dataset, and the assembly error compared with the digital model for each element was derived. The degree of tolerance violation was classified into three levels of severity using the k-means clustering algorithm [51] to provide additional descriptive analytics for decision makers. Finally, the locations of the nodes of the spaceframe were estimated using the least-squares axis-line intersection of the intersecting elements.

The proposed node estimation framework generates the as-built structural model, which can be used to estimate unknown parameters in the governing structural equations, such as the stiffness matrix. Employing this process on temporal static displacement estimation of the nodal coordinates (i.e., estimating the temporal change) can support system identification and finite element model calibration in digital twin applications (calibration of digital twins) [59].

VI. RESULTS AND DISCUSSIONS

A. EXPERIMENT #1 RESULTS: INDIVIDUAL PREFABRICATED ELEMENTS

Results of the simulations (metrics of Equation (12), namely, $Precision_{\%}$, $Recall_{\%}$, $Accuracy_{\%}$, $F_{Measure_{\%}}$, computation time (in minutes), and $R_{RMSE_{\%}}$) using all methods (namely, ICP, SvB, PvB, Bayesian, Genetic, SA, and PS) are shown in Figure 4.

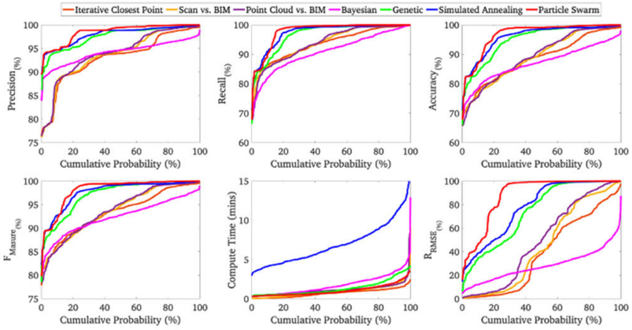

FIGURE 4. Results of Experiment #1: $Precision_{\%}$ (top-left), $Recall_{\%}$ (top-middle), $Accuracy_{\%}$ (top-right), $F_{Measure_{\%}}$ (bottom-left), compute time (bottom-middle), and $R_{RMSE_{\%}}$ (bottom-right).

From the derived results, the following observations were made:

- *Object detection quality*: the best to worst methods were PS, SA, Genetic, PvB, SvB, and ICP. Bayesian performed worse than Genetic, SA and PS in all simulations, and sometimes performed better (less than 50% of the simulations) than PvB.
- *Fitting accuracy*: PS, SA, Genetic, PvB, SvB, and ICP, in the order of best to worst performance. In approximately 58% of the cases, the Bayesian performance was poorer than that of ICP.
- *Computation time*: The methods that performed best to worst were ICP, PvB, SvB, PS, Genetic, Bayesian, and SA. SA performed worse due to lack of parallelization.

B. I. EXPERIMENT #1: PERFORMANCE EVALUATION

The metrics presented in Equation (12) were calculated for each method in each of the simulations. As such, for each method 5,000 different sets of metrics were calculated. Table 4 provides the percentage of the relative error [60]–at the median–of each metric obtained between each method and that of the best method. As such, zero represents the best method and any value higher than zero quantifies the relative error between that method's metrics compared to the best performing (in that category). In other words, lower values are considered better. Table 4 suggests that PS performed the best amongst all methods in terms of detection quality (precision, recall and accuracy) and relative RMSE, followed by SA and Genetic. In terms of runtime, ICP performed the best followed by PvB and PS.

TABLE 4. Experiment #1: Performance evaluation.

Method	Precision (%)	Recall (%)	Accuracy (%)	R_{RMSE} (%)	Time (%)
ICP	5.6	4.7	9.5	61.6	**0.0**
SvB	5.1	3.8	8.6	59.1	31.0
PvB	4.8	2.8	7.6	49.5	5.0
Baysian	4.9	7.8	11.6	73.2	110.6
Genetic	0.6	0.3	0.8	14.3	77.5
SA	0.6	0.3	0.6	6.2	478.9
PS	**0.0**	**0.0**	**0.0**	**0.0**	27.9

* Lower values represent better results; bold represents the best results.

Given the many simulations, the comparative performance of the methods must be evaluated probabilistically to provide a true representation of the capabilities of the methods for the proposed scan-to-QC framework. As such, the stochastic multi-criteria decision-making (MCDM) method presented in [23] was adopted to systematically select the most suitable method probabilistically. This stochastic method requires only the rank ordering of the importance of each criterion. In this study, the following ranking was utilized for the analysis: $R_{RMSE_{\%}} > F_{Measure_{\%}} \geq Accuracy_{\%} \geq Recall_{\%} \geq Precision_{\%} > T_C$.

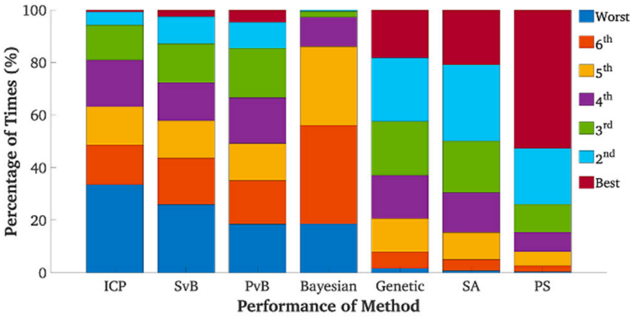

FIGURE 5. Results of the stochastic MCDM [23] based on the considered relative importance of criteria.

Figure 5 represents the percentage of times each method was ranked (from best to worst) based on the stochastic scores. The results show that PS outperformed the rest in over 53% of the simulations, over 2.5 and 2.9 times that achieved by the second and third best methods, the SA and the Genetic, respectively. The higher performance of PS is also consistent with previous studies in BIM-based model fitting [25],

[41]. Some reasons for the higher performance of PS may be attributed to: (i) the directional nature of the velocities (or probabilistic movement) in PS, resembling gradient-like progression [61]; (ii) easier and comparatively less tuning parameters [62]; and (iii) faster convergence with parallel evaluations [63]. Based on the stochastic analysis, the order of the methods from the most suitable to the least was found to be PS, SA, Genetic, PvB, SvB, ICP, and Bayesian.

VII. EXPERIMENT #1: IMPACT OF ELEMENT TYPE

Figure 6 shows the $F_{Measure}$, computation time, and R_{RMSE} performance for the five types of elements considered in this study (Figure 4a–4f). The error bars show the 25th, 50th (median), and 95th percentiles, respectively.

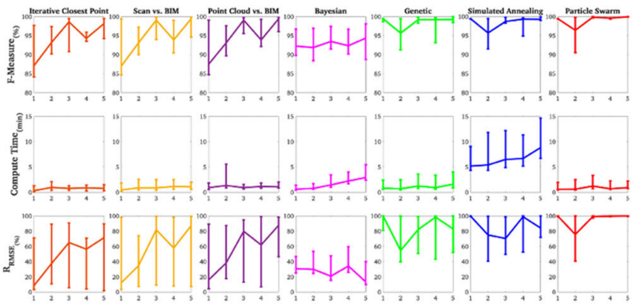

FIGURE 6. Results of the $F_{Measure_{(\%)}}$ (top), compute time (middle), and $R_{RMSE_{\%}}$ (bottom) vs. the element number (Figure 3) for the methods (from left to right), ICP SvB, PvB, Bayesian, Genetic, SA, and PS.

Based on the results of Figure 6, the following observations were made:

- *Deterministic and heuristic methods*: ICP, SvB, and PvB) performed poorly on element #1 in terms of $F_{Measure}$ and R_{RMSE}. This was likely due to the higher number of outliers in element #1. These methods also exhibited similar error patterns at the median for all element types.
- *Baysian*: performed similarly on all elements and was visibly poorer than the other methods, Genetic, SA, and PS, in terms of $F_{Measure}$ and R_{RMSE}. In contrast, Bayesian performed better than ICP, SvB, and PvB in element #1, but poorer in all other elements.
- *Genetic, SA and PS*: performed well on elements #1 and #4, with the most outliers. All the methods appeared to perform relatively poorly on element #2 owing to the missing data of the parallel web, leading to higher rates of local convergence. For PS, the poorer performance at element #2 was explained by the choice of the threshold, which will be discussed in the next section. PS outperformed SA and genetics on elements #3 and #5.

VIII. EXPERIMENT #1: IMPACT OF THRESHOLD

Figure 7 shows the impact of tunable thresholds (Section IV-A.II) for all methods on the $F_{Measure}$, compute time, and R_{RMSE}. The results presented in Figures 4–6 set tunable parameter for the ICP, SvB and PvB, D_{Thresh}, at 20 cm, here, for consistency, the D_{Thresh} parameter was also changed from 5 cm to 20 cm in 5 cm increments.

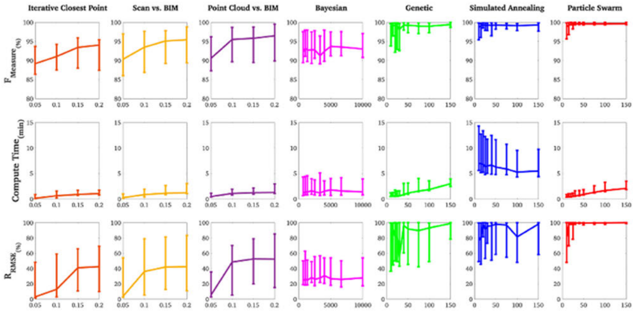

FIGURE 7. Results of the $F_{Measure_{(\%)}}$ (top), compute time (middle), and $R_{RMSE_{\%}}$ (bottom) vs. tunable thresholds (Table 1) for the methods (from left to right), ICP SvB, PvB, Bayesian, Genetic, SA, and PS.

Based on the results of Figure 7, the following noteworthy observations were made:

- *Deterministic and heuristic methods*: ICP, SvB, and PvB improved as D_{Thresh} increased from 5 cm to 20 cm in $F_{Measure}$ and R_{RMSE}. However, no considerable change was observed between the 15 cm and 20 cm thresholds.
- *Baysian*: increasing the maximum number of evaluations to convergence did not appear to considerably impact the Bayesian results.
- *Parameter* G_n: the performance of Genetic, SA and PS improved as the tunable parameter increased.
- *Element #2*: The results of Figure 7 demonstrate that when $G_n \geq 30$, PS at the 25th percentile achieved $F_{Measure}$ and R_{RMSE} compliance of approximately 99% and 96%, respectively. Because the computation time increases as G_n increases, setting PS to $G_n = 30$ provides the optimal balance between accuracy and computation time for the point cloud data used in this study.

For demonstration purposes, Figure 8 shows the final transformed and detected points using each method for a sample rigid body transformation on each of the five elements, with D_{Thresh} and G_n set as 20 cm and 30, respectively.

A. EXPERIMENT #2 RESULTS: SPACEFRAME STRUCTURE

Figure 9 shows the results of assembly verification using the method proposed in Algorithm 1. Based on Experiment #1, the PS algorithm with a swarm size of 30 was employed. Figure 9a shows the assembly error for each element, color-coded using a heat map. The assembly error was calculated as the total RMSE between the inlier points in the original point cloud, and then after recovery of the transformation parameters. This scalar RMSE was then converted into the jet color scheme for visualization and descriptive analytics.

Figure 9b shows the results of the same assembly error of Figure 9a, classified within three severity categories: high severity (in red), medium severity (in yellow), and low severity (in green). Here, red, yellow and green were derived through the k-means clustering algorithm. It is to mention that this figure can be similarly generated through real tolerance thresholds obtained from standard code of practice, or those set within the project's technical specifications [64].

Furthermore, the reported tolerance violation classification can act as one factor among many that predict the element's reliability, criticality, or vulnerability. These may include engineering design factors, such as stiffness sensitivity, redundancy, betweenness centrality, damage sensitivity, and force flux to offer a more accurate depiction of the impact of the element's tolerance violation on the overall structural integrity. Decision-makers can then utilize this information to devise data-informed rectification plans to minimize rework by estimating the time demand of each element and prioritize the elements (to be repaired) based on their multifactorial severity [65]. For further visual reference, Figures 9c–9f show the results for the three most out-of-tolerance elements.

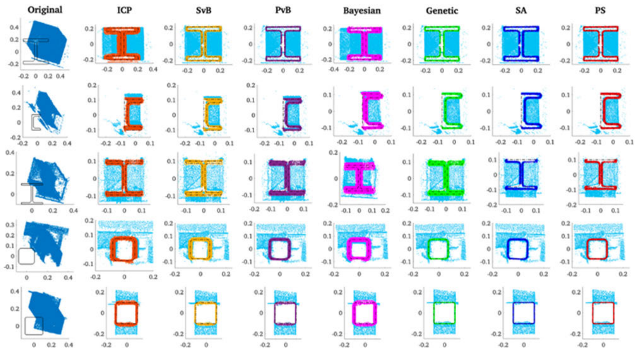

FIGURE 8. **Results of the element detection for element #1–#5 in Figure 4 subjected to rigid body transformation for the methods–from left to right, ICP, SvB, PvB, Bayesian, Genetic, SA and PS.**

B. I. EXPERIMENT #2: VALIDATION

To report on the overall performance of the methodology for on-site assembly verification, the estimated nodal coordinates were compared to those of the ground truth. Figure 10a shows the estimated nodal coordinates of the space frame. The nodal coordinates were estimated through least squares intersection [66] of the 3D axis line of the elements sharing the same node. The 3D axis line was estimated as the inverse transformation–obtained from Algorithm 1–of the element's 3D axis line in the planned BIM. Given that the nodal coordinates cannot be directly measured through an external instrument (e.g., a total station), the ground truth, here, was derived by using the individual element's ground truth transformations obtained through the manual process of Experiment #1 (described in Section III-A.II). The maximum error, mean radial spherical error (MRSE) and offset between the estimated (proposed method) and ground truth estimates of the nodal coordinates were 1.4 mm, 0.6 mm, and 0.2 mm, respectively. As such, even the maximum deviation was well within the expected instrument's measurement uncertainty. The results indicated strong agreement between the automatic estimation of the nodal coordinates compared to the ground truth.

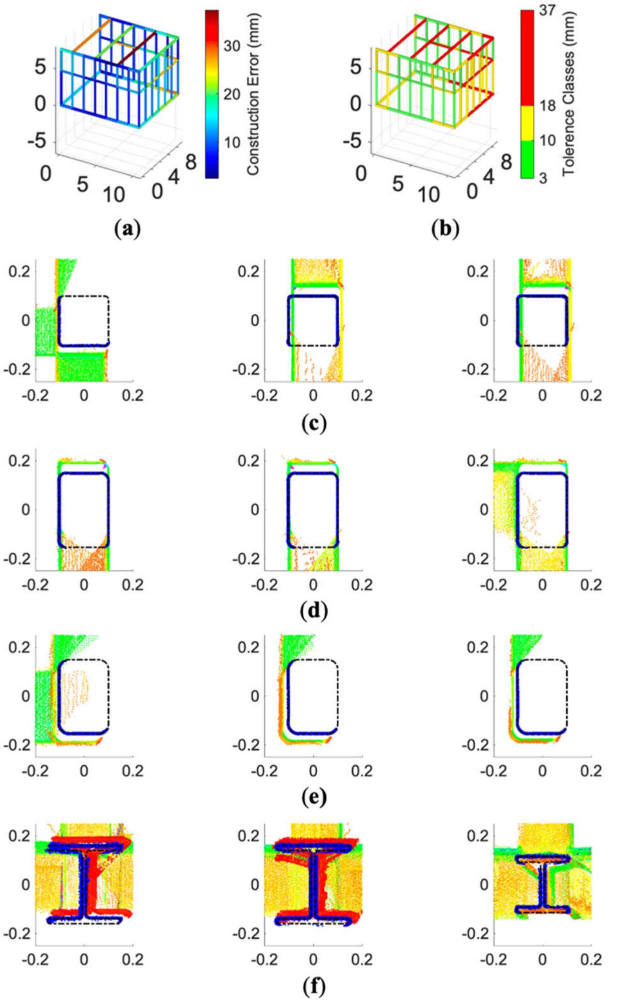

(a) (b)

(c)

(d)

(e)

(f)

FIGURE 9. **Results of the assembly verification using algorithm I: (a) element assembly error with colormap; and (b) tolerance violation based on high (red), medium (yellow) and low (green) severity. Assembly verification before and after transformation for most severe elements: (c) S–HSS; (d)–(e) R_HSS with different fillet; and (f) W–sections.**

Given that each estimated ground truth and nodal coordinates contained measurement uncertainty, the reliability of the estimated nodal coordinates was validated, stochastically. This was accomplished through the standard chi-squared consistency test by adopting the first-order covariance matrices (from uncertainty propagation) as the measure of uncertainty. To this end, the Mahalanobis distance between the estimated nodal coordinates and the ground truth were calculated. This Mahalanobis distance is synonymous with the squared z-score, presented in Equation (8). As such, the probability of violation for each nodal coordinate (p-value) was defined as the upper tail probability where the chi-squared random variable with degree 3 (for the three Cartesian coordinates) was larger than the Mahalanobis distance. Similar to Equation (9), the nodes that fall within the chi-squared cumulative probability with confidence of 95% were considered reliable.

The results of the reliability analysis are shown in Figure 10b. In Figure 10b the colormap of both the nodes and elements represent the accuracy of the estimated compared

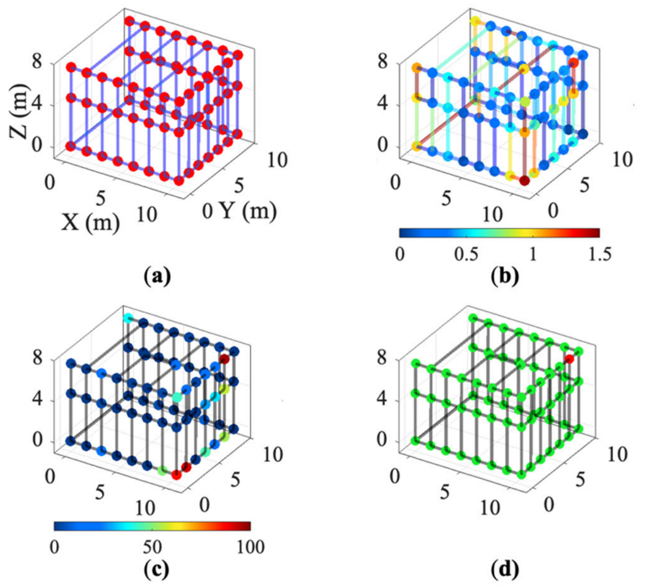

(a) (b) (c) (d)

FIGURE 10. **Reliability of methodology on real spaceframe structure based on stochastic consistency testing: (a) estimated nodal coordinates; (b) accuracy of estimated nodal coordinates and elements compared to ground truth (color bar units in millimeters); (c) p-value for reliability violation (color bar units in %); and (d) reliable (green) and unreliable (red) node estimation based on 95% confidence.**

to the ground truth. Figure 10c represents the p-value–i.e., the probability of violating the consistency test, for each of the estimated nodal coordinates. The larger the nodal values, the higher the probability of violation. Figure 10d shows the binary reliability map of the estimated nodal coordinates. Here, p-values of larger than 95% are considered as unreliable measurements (shown in red). As demonstrated, among the 65 nodal coordinates estimated from 107 element transformations, only “1” was deemed unreliable when considering the combined ground truth and estimated uncertainties. It is still worth noting that the nominal value of the accuracy was within 1.4 mm compared to the best achievable on all 65 nodes. We conclude that the proposed methodology is 98.5% reliable on the presented dataset.

IX. CONCLUSION

This study presents a new formulation for detecting point clouds corresponding to prefabricated (quality-controlled) elements as the solution to a robust AI-based model fitting problem. To this end, the CAD or BIM of the element’s cross-section was approximated as a continuous (and double differentiable) TP. A new set of formulations for the orthogonal fitting of points to the TP function was derived, which was then solved iteratively using the Levenberg-Marquardt algorithm. The method then employed CS to iteratively remove the outlying observations. Given that the success of the CS method is contingent on a “good” initial transformation, the effectiveness of seven methods, namely ICP, SvB, PvB, Bayesian, Genetic, SA, and PS, in recovering the initial transformation parameters was extensively evaluated. To this end, a new objective function was formulated to account for three metrics when fitting TPs to neighboring point clouds, namely, the best-fit error, element’s coverage, and point density in the element’s longitudinal axis.

The methodology was validated and verified on a selected set of five typical prefabricated steel elements and a real-world cantilever steel spaceframe structure. For the single-element case, the five element types with non-analytic cross-sectional geometries were two W-sections, MC–section, R–HSS, and S–HSS. The cross-sectional geometries of these sections. The point clouds of these five prefabricated elements were then subjected to 1,000 random rigid-body transformations. The results of each of the five methods to recover the transformation parameters were compared with those of the ground truth. It was observed that PS with a swarm size greater than 30 could provide near-optimal results for all considered transformations with over 96% and 99% compliance regarding RMSE (fitting accuracy) and object detection quality at the 25th percentile, respectively.

Experiment 2 involved the automatic assembly verification of the prefabricated steel members in a cantilever spaceframe structure from the TLS point clouds. The calibrated PS algorithm with a swarm size of 30 (from the previous experiment) was employed to further illustrate the implications of the proposed methodology in real-world applications. The nodal coordinates of each joint were then estimated and compared with that of the ground truth. The thorough reliability analysis revealed that the accuracies of the nodal coordinates were within 1.4 mm for all 65 estimated nodal coordinates compared to the best achievable through brute force. Furthermore, stochastic consistency tests revealed that–when considering the uncertainties in the measurements– 64 out of 65 nodes were estimated reliability with 95% confidence. This suggested that the proposed method achieved 98.5% reliability in the estimated nodal coordinates for the real-world spaceframe structure.

Although the results presented in this study show promise for the proposed methodology, the findings of the study open the following new opportunities for future research and development:

1) VARIABLE CROSS-SECTIONS

Here, the problem of elements with fixed cross sections was considered. However, the formulations can be easily extended to 3D and to include scaling. Therefore, future studies in this area are possible, and the effectiveness of these methods must be evaluated.

2) DIMENSIONAL ERRORS

The application of new methods for transfer, reinforcement, and deep learning, combined with the methods presented here, may provide robust solutions to the complex problem of point cloud processing for elements with dimensional errors, such as large plastic deformations, shearing, and erroneous builds.

3) TECHNOLOGY READINESS

Given the promising results of the methodology, future research on the practical application of the proposed method to replace current industry best practices becomes crucial. Among such research, scoring the technology readiness level (TRL) as well as feedback from professional bodies within the industry are avenues for further development.

APPENDIX A
CLOSED-FORM JACOBIAN

The Jacobian of the objective function in Equation (6) with respect to the geometric parameter vector $\rho = (x_c, y_c, \theta)$ is obtained analytically as follows:

$$\begin{cases} \dfrac{\partial D_{X,t}}{\partial \rho} = \dfrac{\partial X}{\partial \rho} - \dfrac{\partial f_{X,t}}{\partial \rho} \\ \dfrac{\partial D_{Y,t}}{\partial \rho} = \dfrac{\partial Y}{\partial \rho} - \dfrac{\partial f_{Y,t}}{\partial \rho} \\ \dfrac{\partial X}{\partial \rho} = (-C, -S, Y) \\ \dfrac{\partial Y}{\partial \rho} = (S, -C, -X) \\ \dfrac{\partial f_{X,t}}{\partial \rho} = f'_{X,t} \cdot \dfrac{\partial t}{\partial \rho} \\ \dfrac{\partial f_{Y,t}}{\partial \rho} = f'_{Y,t} \cdot \dfrac{\partial t}{\partial \rho} \\ \dfrac{\partial t}{\partial \rho} = -\dfrac{f'_{X,t} \cdot \frac{\partial X}{\partial \rho} + f'_{Y,t} \cdot \frac{\partial Y}{\partial \rho}}{g'_{X,Y,t}} \end{cases} \tag{13}$$

APPENDIX B
CLOSED-FORM DERIVATIVE OF TP FUNCTION

$$\begin{cases} f'_{X,t} = \dfrac{df_{X,t}}{dt} = \sum_{k=1}^{n} ka_{kX}\cos(kt) - kb_{kX}\sin(kt) \\ f'_{Y,t} = \dfrac{df_{Y,t}}{dt} = \sum_{k=1}^{n} ka_{kY}\cos(kt) - kb_{kY}\sin(kt) \\ f''_{X,t} = \dfrac{d^2 f_{X,t}}{dt^2} = \sum_{k=1}^{n} -k^2 a_{kX}\sin(kt) - k^2 b_{kX}\cos(kt) \\ f''_{Y,t} = \dfrac{d^2 f_{Y,t}}{dt^2} = \sum_{k=1}^{n} -k^2 a_{kY}\sin(kt) - k^2 b_{kY}\cos(kt) \end{cases} \tag{14}$$

ACKNOWLEDGMENT

The authors wish to acknowledge the generous endowment provided by GOLDBECK GmbH to Karlsruhe Institute of Technology (KIT) to establish the Chair for Digital Engineering and Construction (DEC) at the Institute for Technology and Management in Construction (TMB). The authors wish to acknowledge the support provided by the KIT Publication Fund of the Karlsruhe Institute of Technology in supplying the APC. This research received no additional external funding.

REFERENCES

[1] (2024). *Prefabricated Structure Industry 2024*. Accessed: Dec. 16, 2024. [Online]. Available: https://www.reportlinker.com/market-report/Building-Products/483302/Prefabricated-Structure

[2] V. Tavares, J. Gregory, R. Kirchain, and F. Freire, "What is the potential for prefabricated buildings to decrease costs and contribute to meeting EU environmental targets?" *Building Environ.*, vol. 206, Dec. 2021, Art. no. 108382, doi: 10.1016/j.buildenv.2021.108382.

[3] W. Shahzad, J. Mbachu, and N. Domingo, "Marginal productivity gained through prefabrication: Case studies of building projects in Auckland," *Buildings*, vol. 5, no. 1, pp. 196–208, Feb. 2015, doi: 10.3390/buildings5010196.

[4] N. Bertram, S. Fuchs, J. Mischke, R. Palter, G. Strube, and J. Woetzel, "Modular construction: From projects to products," *Capital Projects Infrastruct.*, pp. 10–11, Jun. 2019. [Online]. Available: https://www.mckinsey.com/capabilities/operations/our-insights/modular-construction-from-projects-to-products

[5] L. Jaillon, C. S. Poon, and Y. H. Chiang, "Quantifying the waste reduction potential of using prefabrication in building construction in Hong Kong," *Waste Manage.*, vol. 29, no. 1, pp. 309–320, Jan. 2009, doi: 10.1016/j.wasman.2008.02.015.

[6] J. Hong, G. Q. Shen, C. Mao, Z. Li, and K. Li, "Life-cycle energy analysis of prefabricated building components: An input–output-based hybrid model," *J. Cleaner Prod.*, vol. 112, pp. 2198–2207, Jan. 2016, doi: 10.1016/j.jclepro.2015.10.030.

[7] F. Greer and A. Horvath, "Modular construction's capacity to reduce embodied carbon emissions in California's housing sector," *Building Environ.*, vol. 240, Jul. 2023, Art. no. 110432, doi: 10.1016/j.buildenv.2023.110432.

[8] R. Maalek, D. D. Lichti, R. Walker, A. Bhavnani, and J. Y. Ruwanpura, "Extraction of pipes and flanges from point clouds for automated verification of pre-fabricated modules in oil and gas refinery projects," *Autom. Construct.*, vol. 103, pp. 150–167, Jul. 2019, doi: 10.1016/j.autcon.2019.03.013.

[9] N. Galvão, J. C. Matos, R. Hajdin, L. Ferreira, and M. G. Stewart, "Impact of construction errors on the structural safety of a post-tensioned reinforced concrete bridge," *Eng. Struct.*, vol. 267, Sep. 2022, Art. no. 114650, doi: 10.1016/j.engstruct.2022.114650.

[10] T. Hillman Willis and W. D. Willis, "A quality performance management system for industrial construction engineering projects," *Int. J. Quality Rel. Manage.*, vol. 13, no. 9, pp. 38–48, Dec. 1996, doi: 10.1108/02656719610150605.

[11] M. Golparvar-Fard, F. Peña-Mora, and S. Savarese, "Automated progress monitoring using unordered daily construction photographs and IFC-based building information models," *J. Comput. Civil Eng.*, vol. 29, no. 1, Jan. 2015, Art. no. 04014025, doi: 10.1061/(asce)cp.1943-5487.0000205.

[12] Y. Pan, A. Braun, I. Brilakis, and A. Borrmann, "Enriching geometric digital twins of buildings with small objects by fusing laser scanning and AI-based image recognition," *Autom. Construct.*, vol. 140, Aug. 2022, Art. no. 104375, doi: 10.1016/j.autcon.2022.104375.

[13] F. Bosché, "Automated recognition of 3D CAD model objects in laser scans and calculation of as-built dimensions for dimensional compliance control in construction," *Adv. Eng. Informat.*, vol. 24, no. 1, pp. 107–118, Jan. 2010, doi: 10.1016/j.aei.2009.08.006.

[14] F. Bosché, M. Ahmed, Y. Turkan, C. T. Haas, and R. Haas, "The value of integrating scan-to-BIM and scan-vs-BIM techniques for construction monitoring using laser scanning and BIM: The case of cylindrical MEP components," *Autom. Construct.*, vol. 49, pp. 201–213, Jan. 2015, doi: 10.1016/j.autcon.2014.05.014.

[15] J. Li, Q. Hu, Y. Zhang, and M. Ai, "Robust symmetric iterative closest point," *ISPRS J. Photogramm. Remote Sens.*, vol. 185, pp. 219–231, Mar. 2022, doi: 10.1016/j.isprsjprs.2022.01.019.

[16] D. P. Kroese, T. Brereton, T. Taimre, and Z. I. Botev, "Why the Monte Carlo method is so important today," *WIREs Comput. Statist.*, vol. 6, no. 6, pp. 386–392, Nov. 2014, doi: 10.1002/wics.1314.

[17] R. Maalek, "Field information modeling (FIM): Best practices using point clouds," *Remote Sens.*, vol. 13, no. 5, p. 967, Mar. 2021, doi: 10.3390/rs13050967.

[18] A. Dittrich, M. Weinmann, and S. Hinz, "Analytical and numerical investigations on the accuracy and robustness of geometric features extracted from 3D point cloud data," *ISPRS J. Photogramm. Remote Sens.*, vol. 126, pp. 195–208, Apr. 2017, doi: 10.1016/j.isprsjprs.2017.02.012.

[19] M. Nahangi and C. T. Haas, "Automated 3D compliance checking in pipe spool fabrication," *Adv. Eng. Informat.*, vol. 28, no. 4, pp. 360–369, Oct. 2014, doi: 10.1016/j.aei.2014.04.001.

[20] M.-M. Sharif, M. Nahangi, C. Haas, and J. West, "Automated model-based finding of 3D objects in cluttered construction point cloud models," *Comput.-Aided Civil Infrastruct. Eng.*, vol. 32, no. 11, pp. 893–908, Nov. 2017, doi: 10.1111/mice.12306.

[21] A. Dimitrov and M. Golparvar-Fard, "Segmentation of building point cloud models including detailed architectural/structural features and MEP systems," *Autom. Construct.*, vol. 51, pp. 32–45, Mar. 2015, doi: 10.1016/j.autcon.2014.12.015.

[22] M. Weinmann, B. Jutzi, S. Hinz, and C. Mallet, "Semantic point cloud interpretation based on optimal neighborhoods, relevant features and efficient classifiers," *ISPRS J. Photogramm. Remote Sens.*, vol. 105, pp. 286–304, Jul. 2015, doi: 10.1016/j.isprsjprs.2015.01.016.

[23] R. Maalek and S. Maalek, "Repurposing existing skeletal spatial structure (SkS) system designs using the field information modeling (FIM) framework for generative decision-support in future construction projects," *Sci. Rep.*, vol. 13, no. 1, p. 19591, Nov. 2023, doi: 10.1038/s41598-023-46523-z.

[24] R. Maalek, D. Lichti, and J. Ruwanpura, "Robust segmentation of planar and linear features of terrestrial laser scanner point clouds acquired from construction sites," *Sensors*, vol. 18, no. 3, p. 819, Mar. 2018, doi: 10.3390/s18030819.

[25] F. Noichl, Y. Pan, and A. Borrmann, "Automated steel structure model reconstruction through point cloud instance segmentation and parametric shape fitting," *J. Inf. Technol. Construct.*, vol. 30, pp. 1099–1122, Jul. 2025, doi: 10.36680/j.itcon.2025.045.

[26] J. Won Ma, J. Jung, and F. Leite, "Deep learning–based scan-to-BIM automation and object scope expansion using a low-cost 3D scan data," *J. Comput. Civil Eng.*, vol. 38, no. 6, Nov. 2024, Art. no. 04024040, doi: 10.1061/jccee5.cpeng-5751.

[27] M. Hubert, M. Debruyne, and P. J. Rousseeuw, "Minimum covariance determinant and extensions," *WIREs Comput. Statist.*, vol. 10, no. 3, May 2018, Art. no. e1421, doi: 10.1002/wics.1421.

[28] Y. Yan and J. F. Hajjar, "Geometric models from laser scanning data for superstructure components of steel girder bridges," *Autom. Construct.*, vol. 142, Oct. 2022, Art. no. 104484, doi: 10.1016/j.autcon.2022.104484.

[29] Y. Li, I. Nolte, M. Vasios, V. Voev, and Q. Xu, "Weighted least squares realized covariation estimation," *J. Banking Finance*, vol. 137, Apr. 2022, Art. no. 106420, doi: 10.1016/j.jbankfin.2022.106420.

[30] R. Maalek and D. D. Lichti, "Robust detection of non-overlapping ellipses from points with applications to circular target extraction in images and cylinder detection in point clouds," *ISPRS J. Photogramm. Remote Sens.*, vol. 176, pp. 83–108, Jun. 2021, doi: 10.1016/j.isprsjprs.2021.04.010.

[31] R. Maalek and D. D. Lichti, "New confocal hyperbola-based ellipse fitting with applications to estimating parameters of mechanical pipes from point clouds," *Pattern Recognit.*, vol. 116, Aug. 2021, Art. no. 107948, doi: 10.1016/j.patcog.2021.107948.

[32] D. Simon, *Evolutionary Optimization Algorithms*, 1st ed. Wiley, 2013, pp. 179–220.

[33] J. Mockus, "Application of Bayesian approach to numerical methods of global and stochastic optimization," *J. Global Optim.*, vol. 4, no. 4, pp. 347–365, Jun. 1994, doi: 10.1007/bf01099263.

[34] D. Whitley, "A genetic algorithm tutorial," *Statist. Comput.*, vol. 4, no. 2, pp. 65–85, Jun. 1994, doi: 10.1007/bf00175354.

[35] I. O. Bohachevsky, M. E. Johnson, and M. L. Stein, "Generalized simulated annealing for function optimization," *Technometrics*, vol. 28, no. 3, pp. 209–217, Aug. 1986, doi: 10.1080/00401706.1986.10488128.

[36] J. Kennedy and R. Eberhart, "Particle swarm optimization," in *Proc. Int. Conf. Neural Netw. (ICNN)*, vol. 4, Dec. 1995, pp. 1942–1948, doi: 10.1109/ICNN.1995.488968.

[37] M. Tsionas, "Bayesian inference using least median of squares and least trimmed squares in models with independent or correlated errors and outliers," *Commun. Statist. Theory Methods*, vol. 53, no. 16, pp. 5761–5772, Aug. 2024, doi: 10.1080/03610926.2023.2232905.

[38] C. L. Karr, B. Weck, D. L. Massart, and P. Vankeerberghen, "Least median squares curve fitting using a genetic algorithm," *Eng. Appl. Artif. Intell.*, vol. 8, no. 2, pp. 177–189, Apr. 1995, doi: 10.1016/0952-1976(94)00064-t.

[39] A. Rusiecki, "Robust learning algorithm based on iterative least median of squares," *Neural Process. Lett.*, vol. 36, no. 2, pp. 145–160, Oct. 2012, doi: 10.1007/s11063-012-9227-z.

[40] H. Shinzawa, J.-H. Jiang, M. Iwahashi, and Y. Ozaki, "Robust curve fitting method for optical spectra by least median squares (LMedS) estimator with particle swarm optimization (PSO)," *Anal. Sci.*, vol. 23, no. 7, pp. 781–785, Jul. 2007, doi: 10.2116/analsci.23.781.

[41] M. S. Mafipour, S. Vilgertshofer, and A. Borrmann, "Automated geometric digital twinning of bridges from segmented point clouds by parametric prototype models," *Autom. Construct.*, vol. 156, Dec. 2023, Art. no. 105101, doi: 10.1016/j.autcon.2023.105101.

[42] F. Noichl, Y. Pan, M. S. Mafipour, A. Braun, I. Brilakis, and A. Borrmann, "From enriched point cloud to structural and MEP models: An automated approach to create semantic-geometric models for industrial facilities," in *Proc. Comput. Civil Eng.*, Jan. 2024, pp. 92–99, doi: 10.1061/9780784485224.012.

[43] L. Barazzetti, "Parametric as-built model generation of complex shapes from point clouds," *Adv. Eng. Informat.*, vol. 30, no. 3, pp. 298–311, Aug. 2016, doi: 10.1016/j.aei.2016.03.005.

[44] S. J. Ahn, *Least Squares Orthogonal Distance Fitting of Curves and Surfaces in Space* (Lecture Notes in Computer Science), 1sty ed. Springer, 2004, doi: 10.1007/b104017.

[45] C. T. Zahn and R. Z. Roskies, "Fourier descriptors for plane closed curves," *IEEE Trans. Comput.*, vol. C-21, no. 3, pp. 269–281, Mar. 1972, doi: 10.1109/TC.1972.5008949.

[46] V. Guruswami and D. Zuckerman, "Robust Fourier and polynomial curve fitting," in *Proc. IEEE 57th Annu. Symp. Found. Comput. Sci. (FOCS)*, Oct. 2016, pp. 751–759, doi: 10.1109/FOCS.2016.75.

[47] A. Lucas, "Ising formulations of many NP problems," *Frontiers Phys.*, vol. 2, pp. 1–14, Feb. 2014, doi: 10.3389/fphy.2014.00005.

[48] D. Comaniciu and P. Meer, "Mean shift: A robust approach toward feature space analysis," *IEEE Trans. Pattern Anal. Mach. Intell.*, vol. 24, no. 5, pp. 603–619, May 2002, doi: 10.1109/34.1000236.

[49] C. Leys, C. Ley, O. Klein, P. Bernard, and L. Licata, "Detecting outliers: Do not use standard deviation around the mean, use absolute deviation around the median," *J. Experim. Social Psychol.*, vol. 49, no. 4, pp. 764–766, Jul. 2013, doi: 10.1016/j.jesp.2013.03.013.

[50] D. L. Olson and D. Delen, *Advanced Data Mining Techniques*. Cham, Switzerland: Springer, 2008, doi: 10.1007/978-3-540-76917-0.

[51] D. Arthur and S. Vassilvitskii, "K-means++: The advantages of careful seeding," in *Proc. Annu. ACM-SIAM Symp. Discrete Algorithms*, 2007, pp. 1–11. [Online]. Available: https://dl.acm.org/doi/10.5555/1283383.1283494

[52] J. Snoek, H. Larochelle, and R. P. Adams, "Practical Bayesian optimization of machine learning algorithms supplementary materials," in *Proc. NIPS*, 2012, pp. 2951–2959.

[53] M. A. Gelbart, J. Snoek, and R. P. Adams, "Bayesian optimization with unknown constraints," in *Proc. 30th Conf. Uncertainty Artif. Intell. (UAI)*, 2014.

[54] D. E. Goldberg, "Genetic algorithms in search, optimization and machine learning," *Choice Rev. Online*, vol. 27, no. 2, 1988, doi: 10.5860/choice.27-0936.

[55] A. R. Conn, N. Gould, and P. L. Toint, "A globally convergent Lagrangian barrier algorithm for optimization with general inequality constraints and simple bounds," *Math. Comput.*, vol. 66, no. 217, pp. 261–289, Jan. 1997, doi: 10.1090/s0025-5718-97-00777-1.

[56] L. Ingber, "Adaptive simulated annealing (ASA): Lessons learned," *Control Cybern.*, vol. 25, no. 1, 2000.

[57] M. Erik, H. Pedersen, and M. E. H. Pedersen, "Good parameters for particle swarm optimization," Hvass Laboratories, Copenhagen, Denmark, Tech. Rep. HL1001, 2010.

[58] E. Mezura-Montes and C. A. C. Coello, "Constraint-handling in nature-inspired numerical optimization: Past, present and future," *Swarm Evol. Comput.*, vol. 1, no. 4, pp. 173–194, Dec. 2011, doi: 10.1016/j.swevo.2011.10.001.

[59] R. Maalek. (2025). *Digital Twin Calibration Using Point Clouds*. Github. Accessed: Feb. 11, 2025. [Online]. Available: https://github.com/RezMaal/Digital-Twin-Calibration-using-Point-Clouds

[60] R. Maalek and F. Sadeghpour, "Accuracy assessment of ultra-wide band technology in tracking static resources in indoor construction scenarios," *Autom. Construct.*, vol. 30, pp. 170–183, Mar. 2013, doi: 10.1016/j.autcon.2012.10.005.

[61] R. Poli, J. Kennedy, and T. Blackwell, "Particle swarm optimization: An overview," *Swarm Intell.*, vol. 1, no. 1, pp. 33–57, Oct. 2007, doi: 10.1007/s11721-007-0002-0.

[62] M. R. Bonyadi and Z. Michalewicz, "Particle swarm optimization for single objective continuous space problems: A review," *Evol. Comput.*, vol. 25, no. 1, pp. 1–54, Mar. 2017, doi: 10.1162/EVCO_r_00180.

[63] M. Clerc and J. Kennedy, "The particle swarm–explosion, stability, and convergence in a multidimensional complex space," *IEEE Trans. Evol. Comput.*, vol. 6, no. 1, pp. 58–73, Feb. 2002, doi: 10.1109/4235.985692.

[64] D. Ballast, "Construction tolerances," *Construct. Specifier*, vol. 59, no. 11, 2006.

[65] R. Maalek, "New model to minimize cost and time of rework due to prefabricated construction errors," in *Proc. Annu. Conf. Int. Group Lean Construct.*, Jun. 2025, pp. 834–845.

[66] *Least-Squares Intersection of Lines*. Accessed: Oct. 9, 2025. [Online]. Available: https://web.archive.org/web/20170912055605/http://cal.cs.illinois.edu/~johannes/research/LS_line_intersect.pdf

REZA MAALEK is currently an Endowed Industrial Chair and a Junior Professor of digital engineering and construction with Karlsruhe Institute of Technology, sponsored by GOLDBECK GmbH.

Dr. Maalek was a recipient of Alberta Science and Technology (ASTech) Foundation Award for Outstanding Achievement in Applied Technology, in 2018, which is one of the province of Alberta's highest honors in science and technology for his contributions in creating innovative and scientific solutions to practical problems, and pertaining to construction automation. During his M.Sc. and Ph.D. with the University of Calgary.

SHAHROKH MAALEK is currently a retired Professor of civil engineering with the University of Tehran and the President of Iranian Institute of Spatial Structure (IISS).

Prof. Maalek has served on numerous committees for the standard code of practice on steel and concrete. He has also written the national code of practice of spatial structure design and bridge information management of aging infrastructures. Throughout his carrier as an academic, he was a recipient of many awards and recognition for teaching and research excellence, including the prestigious Henry Adams Award by the Institute of Structural Engineers, U.K., in 1991.

• • •